

Theoretical study of charge-transport and optical properties of organic crystals: 4,5,9,10-pyrenediimides

Jin-Dou Huang,^a Kun Yu,^b Xiaohua Huang,^b Dengyi Chen,^b Jing Wen,^b Shibo Cheng^c and Huipeng Ma^{b*}

Received 15 October 2018

Accepted 6 April 2019

Edited by X. Zhang, Tsinghua University, China

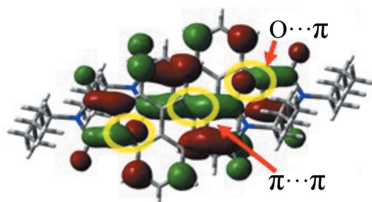
Keywords: pyrenediimides; charge-carrier mobility; time-dependent density functional theory; structure–property relationships.

^aKey Laboratory of New Energy and Rare Earth Resource Utilization of State Ethnic Affairs Commission, School of Physics and Materials Engineering, Dalian Nationalities University, Dalian 116600, People's Republic of China, ^bCollege of Medical Laboratory Science, Dalian Medical University, Dalian 116044, People's Republic of China, and ^cSchool of Chemistry and Chemical Engineering, Shandong University, Jinan 250100, People's Republic of China. *Correspondence e-mail: hpma@dlmedu.edu.cn

This work presents a systematic study of the conducting and optical properties of a family of aromatic diimides reported recently and discusses the influences of side-chain substitution on the reorganization energies, crystal packing, electronic couplings and charge injection barrier of 4,5,9,10-pyrenediimide (PyDI). Quantum-chemical calculations combined with the Marcus–Hush electron transfer theory revealed that the introduction of a side chain into 4,5,9,10-pyrenediimide increases intermolecular steric interactions and hinders close intermolecular π – π stacking, which results in weak electronic couplings and finally causes lower intrinsic hole and electron mobility in *t*-C₅-PyDI ($\mu_h = 0.004 \text{ cm}^2 \text{ V}^{-1} \text{ s}^{-1}$ and $\mu_e = 0.00003 \text{ cm}^2 \text{ V}^{-1} \text{ s}^{-1}$) than in the C₅-PyDI crystal ($\mu_h = 0.16 \text{ cm}^2 \text{ V}^{-1} \text{ s}^{-1}$ and $\mu_e = 0.08 \text{ cm}^2 \text{ V}^{-1} \text{ s}^{-1}$). Furthermore, electronic spectra of C₅-PyDI were simulated and time-dependent density functional theory calculation results showed that the predicted fluorescence maximum of *t*-C₅-PyDI, corresponding to an $S_1 \rightarrow S_0$ transition process, is located at 485 nm, which is close to the experimental value (480 nm).

1. Introduction

Organic semiconductors are of great interest for their intrinsic scientific challenge and potential applications in organic electronic devices such as organic light-emitting diodes (Lin *et al.*, 2016), plastic solar cells (Gao *et al.*, 2017; Skrypnichuk *et al.*, 2016; Yang *et al.*, 2016), organic lasers (Kuehne & Gather, 2016; Zhang *et al.*, 2016), (bio)chemical sensors (Wang *et al.*, 2017; Haughey *et al.*, 2016) and organic field-effect transistors (OFETs) (Zhao *et al.*, 2017; Sung *et al.*, 2016; Raghuvanshi *et al.*, 2016; Matsushima *et al.*, 2016; Ford *et al.*, 2016). Compared with *p*-channel materials, the development of high-performance ambient-stable *n*-channel materials has largely lagged due to the fact that the transport in *n*-channel conductors is degraded easily by air, and their low electronic affinity hinders efficient injection of electrons into the empty lowest unoccupied molecular orbital (LUMO). In recent years, numerous attempts were made to overcome these difficulties, and some new *n*-channel semiconductors have been realized via functionalization of Naphthalene diimides (NDIs) (Bélanger-Chabot *et al.*, 2017; Yuan *et al.*, 2016; Purdum *et al.*, 2016; Kobaisi *et al.*, 2016), diketopyrrolopyrrole (DPP) (Tang *et al.*, 2017; Yao *et al.*, 2016; Li *et al.*, 2016; Yi *et al.*, 2015), perylene diimides (Yue *et al.*, 2014; Liu *et al.*, 2014; Zhang & Zhao, 2012; Wuerthner & Stolte, 2011) and heteroacenes (Xu *et al.*, 2016) with electron-withdrawing substituents or alkyl chains. For



example, Yuan *et al.* synthesized difluoro- and tetrafluoro-substituted Naphthalene diimides, and the OFETs based on these fluorinated NDIs exhibited *n*-channel field-effect character under ambient conditions with a maximum mobility of $0.1 \text{ cm}^2 \text{ V}^{-1} \text{ s}^{-1}$ (Yuan *et al.*, 2016). Klauk and co-workers found that halogen and cyano substituents are ideally suited to tune the DPP dyes' absorption and redox properties into a favorable regime for applications in organic transistors and solar cells, and the alkyl chain substitution could lead to superior π - π contacts between DPP molecules within the layers and closer distances between the DPP layers, both of which are favorable for charge-carrier transport (Stolte *et al.*, 2016). In our previous work, the transport parameters of the cyanated bithiophene-functionalized DPP molecule were simulated in the context of the band model and hopping models, and the theoretical intrinsic electron mobility could reach $2.26 \text{ cm}^2 \text{ V}^{-1} \text{ s}^{-1}$ (Huang *et al.*, 2015). More recently, Zhang *et al.* designed and synthesized a new type of aromatic diimide, pyrene-diimide (PyDI) small molecules (see Fig. 1), which exhibit excellent charge-transport capability and attractive optical properties (Wu *et al.*, 2017). As a potential family of *n*-type organic semiconductors however, there are very few reports on their structure–function relationship and electronic structural properties up to now. A theoretical investigation of the relationship between the nature of the different alkyl groups and device performance, and a prediction of their intrinsic electron-transfer mobility are instrumental in guiding the molecular design and development of novel organic semiconducting materials, which is also the focus of this work.

In this work, the charge-transport and optical properties of 4,5,9,10-pyrenediimides (C_5 -PyDI, C_6 -PyDI, *t*- C_5 -PyDI and *t*- C_6 -PyDI, see Fig. 1) were systematically investigated. Firstly, the reorganization energy associated with charge transport was evaluated using the adiabatic potential energy surface (APS) method, and the influence of the bond-parameter variations on the local electron–vibration coupling were discussed in detail, which evaluates well the effects of different

alkyl groups on the reorganization energy. Then, the structural and electronic properties of C_5 -PyDI, C_6 -PyDI, *t*- C_5 -PyDI and *t*- C_6 -PyDI were investigated, and the angular resolution anisotropic mobility for both electron and hole transport were further evaluated using the newly developed simulation methods. In the end, the steady-state absorption and fluorescence spectra were simulated and a new assignment of fluorescence bands in the experiments is confirmed.

2. Computational methods

2.1. Organization energy, ionization potential and electronic affinity

The reorganization energy λ , associated with the charge-transport process in organic solid materials, can be evaluated in two ways (Zhao & Liang, 2012). The first is the normal-mode (NM) analysis method, which partitions the total relaxation energy into contributions from each vibrational mode:

$$\lambda = \sum \lambda_i = \sum (\omega_i^2 \Delta Q_i^2) / 2, \quad (1)$$

where ΔQ_i represents the displacement along normal mode Q_i between the equilibrium geometries of the neutral and charged molecules; ω_i is the corresponding frequency. The other method is the APS method (the four-point approach), in which λ can be expressed as follows:

$$\lambda = \lambda_1 + \lambda_2 = (E_{\pm}^* - E_{\pm}) + (E^* - E). \quad (2)$$

Here, E and E_{\pm} represent the energies of the neutral and cation/anion species in their lowest energy geometries, respectively; E^* and E_{\pm}^* are the energies of the neutral and cation/anion species with the geometries of the cation/anion and neutral species, respectively. Our previous studies showed that the APS method is suitable for both flexible and rigid molecules; in comparison, the NM analysis is more appropriate for rigid molecules due to the large deviation of the lattice vibration from the harmonic oscillator model for flexible molecules (Ma *et al.*, 2017*a,b*). In this work, we selected the APS method to calculate the reorganization energy.

From the APS of neutral/charged species, the vertical ionization potential (VIP), adiabatic ionization potential (AIP), vertical electronic affinity (VEA) and adiabatic electron affinity (AEA) can be calculated as

$$\text{VIP} = E_{+}^* - E, \quad (3)$$

$$\text{AIP} = E_{+} - E, \quad (4)$$

$$\text{VEA} = E - E_{-}^*, \quad (5)$$

$$\text{AEA} = E - E_{-}. \quad (6)$$

Full-geometry optimizations of the monomer molecules and the reorganization energy calculations are carried out using the B3LYP functional (Lee *et al.*, 1988) in conjunction with the 6-311G** basis set. These calculations are performed with the GAUSSIAN09 package (Frisch *et al.*, 2009).

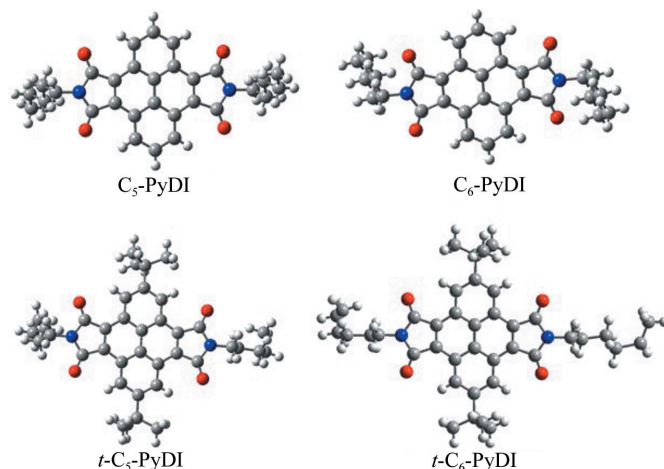


Figure 1
Molecular structures of C_5 -PyDI, C_6 -PyDI, *t*- C_5 -PyDI and *t*- C_6 -PyDI. Red: O; blue: N; gray: C; white: H.

2.2. Electronic coupling

The intermolecular electronic coupling V_{ij} from site i to site j , which describes the overlap of electronic wavefunctions between the donor and acceptor states, can be written as

$$V_{ij} = |J_{ij} - 0.5(e_i + e_j)S_{ij}|/(1 - S_{ij}^2), \quad (7)$$

where S_{ij} , J_{ij} and $e_{i(j)}$ represent the spatial overlap, charge transfer integrals and site energies, respectively. These physical quantities can be calculated as follows:

$$e_{i(j)} = \langle \Psi_{i(j)} | H | \Psi_{i(j)} \rangle, \quad (8)$$

$$S_{ij} = \langle \Psi_i | \Psi_j \rangle, \quad (9)$$

$$J_{ij} = \langle \Psi_i | H | \Psi_j \rangle. \quad (10)$$

Here, H is the Kohn–Sham Hamiltonian of the dimer system and $\Psi_{i(j)}$ represents the monomer HOMOs (for hole transport) or LUMOs (for electron transport) with Löwdin's symmetric transformation, which can be used as the orthogonal basis set for calculation. The calculations of all electronic couplings in different molecular dimers are performed with the PW91/TZVP of density functional theory (DFT) implemented in the Amsterdam density functional (ADF) program (te Velde *et al.*, 2001).

2.3. Anisotropic mobility

The anisotropic mobility is an important intrinsic property of charge transport in organic semiconductors, which depends significantly on the specific surface of organic crystals. Herein, we simulated the angle-resolved charge mobility of 4,5,9,10-pyrenediimides by means of solving the master equation, which has been described in detail elsewhere (Yin & Lv, 2008; Yin *et al.*, 2012). Charge-transfer (CT) kinetics through a solid material with many possible residence sites can be described by the master equation:

$$\frac{dp_i}{dt} = - \sum_{j \neq i} [k_{ij}p_i(1 - p_j) - k_{ji}p_j(1 - p_i)], \quad (11)$$

where k_{ij} is the CT rate constant from site i to site j in the crystal considering the correction of the electronic field, p_i is the charge occupied density on site i , and $1 - p_i$ is the Coulomb penalty factor, which prevents two or more charges at the same time from occupying the same site. If the CT reaches the so-called steady state, $dp_i/dt = 0$, the p_i can be obtained by an efficient iterative procedure given a full set of CT constant k_{ij} values. When an external electric field E is applied to the crystal, the charge will drift accordingly, and the charge mobility m can be determined from the velocity v as the linear response of the motion to the perturbation:

$$\mu = \frac{v}{|E|} = \frac{\sum_{ij} k_{ij}p_i(1 - p_j)\mathbf{R}_{ji}\hat{E}}{p_{\text{tot}}|E|}, \quad (12)$$

where \hat{E} is the unit vector of the applied electric field, \mathbf{R}_{ji} is the vector from site i to site j and p_{tot} is the total charge population in the investigated supercell. The calculation here is performed using the periodic boundary condition with a

Table 1

DFT-B3LYP/6-311G** calculated hole-transfer (λ_h) and electron-transfer (λ_e) reorganization energies of C₅-PyDI, C₆-PyDI, *t*-C₅-PyDI and *t*-C₆-PyDI by the APS approach.

Molecular crystals	λ_h (eV)	λ_e (eV)
C ₅ -PyDI	0.170	0.258
C ₆ -PyDI	0.169	0.257
<i>t</i> -C ₅ -PyDI	0.180	0.251
<i>t</i> -C ₆ -PyDI	0.179	0.251

supercell of size $3 \times 3 \times 3$, and the external electric field E is set to a relatively small value of $1.0 \times 10^{-3} \text{ V \AA}^{-1}$.

2.4. Electronic spectra

As the accuracy of a TDDFT calculation is strongly dependent on the chromophore family, it is essential that TDDFT results are validated by comparing the experimental data prior to a detailed interpretation. The accuracies of different functionals such as B3LYP, PBE0 and M06-2x were assessed by comparing the predicted wavelengths and intensities of the lowest energy bands with experimental absorption data. Our tests showed that the simulated absorption spectra based on the geometry structures optimized using M06-2x are in better agreement with the experimental UV–vis spectra, which is inconsistent with previous studies (Huang *et al.*, 2017a,b, 2018; Ma & Huang, 2016; Yang *et al.*, 2018, 2017). Therefore, the geometry optimizations of *t*-C₅-PyDI at the S_0 state and the S_1 state were implemented using the DFT and TDDFT methods at the M06-2x/TZVP (triple-zeta valence quality with one set of polarization functions) level (Treutler & Ahlrichs, 1995). The self-consistent field convergence thresholds of the energy for both the ground-state and excited-state optimization were used as the default settings (10^{-6}). The excited-state Hessian was obtained by numerical differentiation of analytical gradients using central differences and default displacements of 0.02 Bohr. The geometry optimizations were performed without constraints on bond lengths, angles or dihedral angles. All local minima were confirmed by the absence of an imaginary mode in the vibrational analysis calculations. To evaluate the solvent effect, cyclohexane and chloroform were selected as the solvent in the calculations using the conductor-like screening model (COSMO) method (Klamt & Schüürmann, 1993).

3. Results and discussion

3.1. Reorganization energy

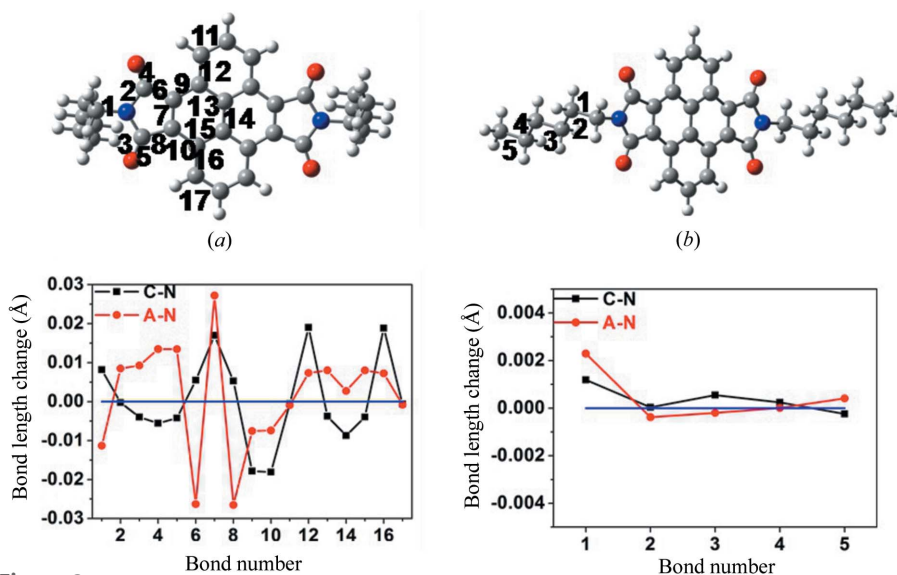
As one of the key parameters influencing the intrinsic charge-transport rates, the reorganization energies evaluated from the four-point approach are collected in Table 1. Comparison of the reorganization energies of C₅-PyDI, C₆-PyDI, *t*-C₅-PyDI and *t*-C₆-PyDI shows that the variation of alkyl chain length has little influence on the reorganization energies associated with intermolecular electron-transfer (λ_e) and intermolecular hole transfer (λ_h), and the introduction of *t*-butyl groups reduces the λ_h and λ_e values no more than

Table 2

Calculated electronic coupling terms V_h (hole transfer) and V_e (electron transfer) for the different hopping pathways in C_5 -PyDI, C_6 -PyDI, t - C_5 -PyDI and t - C_6 -PyDI crystals; r is the intermolecular center-to-center distance.

Molecular crystals	Dimer types	r (Å)	V_h (meV)	V_e (meV)
C_5 -PyDI	P1 = P2	4.880	15.0	17.9
C_6 -PyDI	P1 = P2	4.795	7.2	26.3
t - C_5 -PyDI	P1	4.78	91.1	152.3
	P2	7.796	1.5	0.2
t - C_6 -PyDI	P1	3.519	90.5	145.7
	P2	11.629	0.01	0.01

0.01 eV. For the studied compounds, the λ_e values are much larger than the ones associated with hole-transfer (λ_h). As show in Table 1, the λ_e values of C_5 -PyDI, C_6 -PyDI, t - C_5 -PyDI and t - C_6 -PyDI are 0.258, 0.257, 0.251 and 0.251 eV, respectively, which are about 0.07–0.09 eV larger than the corresponding λ_h values. This indicates that the pyrenediimide framework undergoes larger geometry relaxations during the electron-transfer process. For the sake of comprehensive analysis of the relationship between the molecular structure and the reorganization energy, we display the bond length alternation in the C_6 -PyDI molecule at oxidation and reduction, as shown in Fig. 2. For bonds 1 to 8, as shown in Fig. 2(a), the geometric relaxation occurs predominantly on electron transfer; in contrast, the smaller geometric changes in these bonds on hole transfer contribute less to λ_h , which is consistent with the observation of a larger values of λ_e than λ_h . For C—C bonds 9 to 17 in the pyrene core, the bond relaxation on hole transfer is more pronounced than those on electron transfer [see Fig. 2(a)], which means that the changes in these C—C bond lengths contribute more to λ_h than to λ_e . Combined with the calculated λ_h and λ_e values, it can be concluded that the large λ_e value is mainly attributed to the geometric relaxations of five-membered imide rings and C=O


Figure 2

Calculated variations in the bond lengths of isolated C_6 -PyDI upon oxidation (black symbols) and reduction (red symbols), the x axis represents the chemical bond (C—C, C—O and C—N) number that is marked using different numbers.

bonds rather than the pyrene core. Moreover, the changes in C—C bond length in the alkyl chains are also depicted in Fig. 2(b). All bond-length variations of the C—C bonds between the neutral and charged forms are less than 0.003 Å, suggesting that the geometry relaxations of C—C bonds accompanied with hole and electron transport have a very small effect on their reorganization energies. This explains the small difference in the reorganization energies of C_5 -PyDI, C_6 -PyDI, t - C_5 -PyDI and t - C_6 -PyDI.

3.2. Crystal structure and electronic coupling

In the crystal structures of C_5 -PyDI and C_6 -PyDI, the molecules crystallize in a triclinic system and show a typical one-dimensional π -stacking motif, which is usually considered to exhibit strong π - π interactions and good charge-transport properties. In this motif, only face-to-face intermolecular packing modes can be formed. To facilitate the discussion below, this intermolecular packing mode is defined as the P dimer. For C_5 -PyDI and C_6 -PyDI, the calculated electronic couplings for hole and electron transfer (denoted as V_h and V_e) and the mass-centered distances r in the P dimer are summarized in Table 2. It can be seen that intermolecular electronic couplings are relatively small even though the intermolecular distances are very short. For C_5 -PyDI, the V_h and V_e values are similar, both of which are less than 20 meV; for C_6 -PyDI, the V_e value is 26.3 meV and V_h is only 7.2 meV. In order to understand the weak electronic couplings in the one-dimensional π -stacking motif, the shapes of the HOMOs and LUMOs in the P dimer of C_6 -PyDI are shown in Fig. 3. We can see that the HOMOs and LUMOs are mainly localized on the pyrene core, and the introduction of alkyl chains has little influence on the frontier molecular orbital charge distributions. In contrast to the perfect face-to-face dimer, there exists an obvious displacement between two neighboring molecules

of the P dimer along the molecular axis direction, which leads to a cancellation effect between the bonding and antibonding overlaps and a decrease in the effective coupling projected area. As shown in Fig. 3(b), we can see that the major contribution to the V_h value mainly comes from N $\cdots\pi$ interactions, and $\pi\cdots\pi$ interactions in the P dimer contribute little to the V_h value due to the cancellation effect. In comparison, the distribution character of the LUMO leads to intermolecular O $\cdots\pi$ interactions and partially effective $\pi\cdots\pi$ interactions in the P dimer, as shown in Fig. 3(d), which explains the fact that the V_e value in the P dimer of C_6 -PyDI is about three times larger than the corresponding V_h value. Through the above analysis, we can conclude that the weak electronic couplings in the C_6 -PyDI crystal are mainly due to the large

deviation of the P dimer from perfect face-to-face packing, which results in the compensation of bonding and antibonding interactions.

In the crystal structures of *t*-C₅-PyDI and *t*-C₆-PyDI, the molecules also pack into a lamellar motif; however, every two neighboring molecules form a molecular pair, and the distance between these molecular pairs is much longer than the intermolecular distance within the molecular pair. For example, the distance between *t*-C₆-PyDI pairs is 11.629 Å, and the intermolecular distance in the *t*-C₆-PyDI pair is only 3.519 Å. For the sake of discussion, the dimer with a small intermolecular distance, *i.e.* 3.519 Å, is defined as a P1 dimer; and a dimer with a larger distance, *i.e.* 11.629 Å, is defined as a P2 dimer. Our calculations show that the intermolecular electronic couplings in the P1 dimer are much larger than those in the P2 dimer, which is consistent with the intermolecular distances.

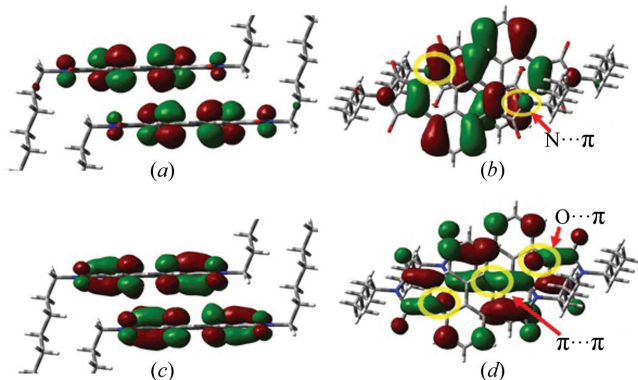


Figure 3 HOMOs (0.02 a.u.) for the P dimer of C₆-PyDI in (a) side view and in (b) top view, and LUMOs (0.02 a.u.) for the P dimer of C₆-PyDI in (c) side view and in (d) top view.

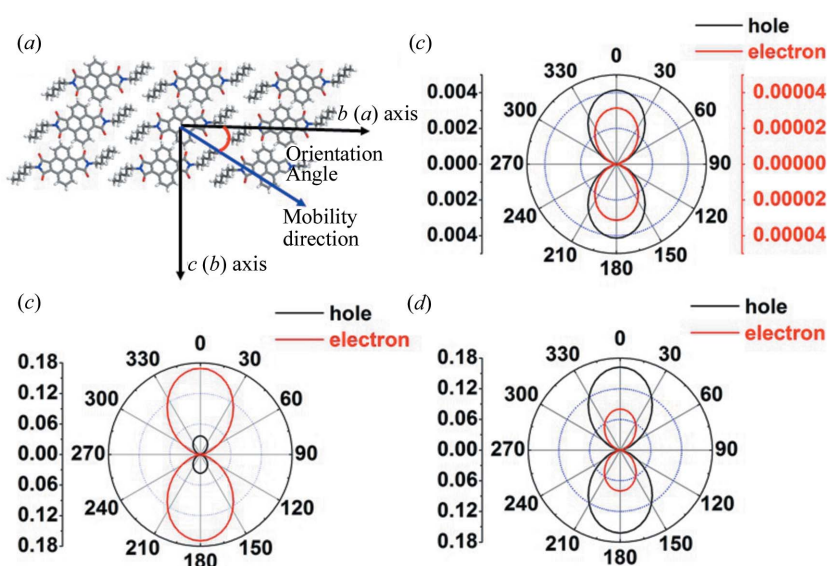


Figure 4 (a) Illustration of the orientation angle of the transistor channel relative to the crystallographic *b* axis for C₅-PyDI and C₆-PyDI and the orientation angle of the transistor channel relative to the crystallographic *a* axis for *t*-C₅-PyDI. Calculated angle-resolved anisotropic hole (black line) and electron (red line) transport mobility as a function of orientation angle for (b) *t*-C₅-PyDI, (c) C₆-PyDI and (d) C₅-PyDI.

Table 3

Theoretical hole-diffusion mobilities (μ_h) and electron-diffusion mobilities (μ_e) of C₅-PyDI, C₆-PyDI and *t*-C₅-PyDI at room temperature ($T = 300$ K), and some experimental charge-transfer mobility values.

	μ_h (theor.)	μ_e (theor.)	μ_e (exp.) [†]
C ₅ -PyDI	0–0.16	0–0.080	0.19 ± 0.13
C ₆ -PyDI	0–0.04	0–0.17	0.29 ± 0.12
<i>t</i> -C ₅ -PyDI	0–0.004	(0–3) × 10 ^{−5}	(8.72 ± 0.91) × 10 ^{−5}

[†] Wu *et al.* (2017).

As shown in Table 2, the V_h and V_e values in the P1 dimer of *t*-C₅-PyDI are 91.1 and 152.3 meV, respectively, which are much stronger than those in the P2 dimer (1.5 and 0.2 meV); similarly, the V_h and V_e values in the P1 dimer of *t*-C₆-PyDI are 90.5 and 145.7 meV, respectively; in comparison, both V_h and V_e values in the P2 dimer are less than 0.01 meV. In this case, the hole/electron transport mobility is primarily determined by the hopping rate between different P1 dimers. The weak electronic couplings in the P2 dimers of *t*-C₅-PyDI and *t*-C₆-PyDI explain their poor OFET properties.

3.3. Anisotropic mobility

The anisotropic hole-transfer and electron-transfer mobility values in the single crystals of C₆-PyDI and C₅-PyDI are shown in Fig. 4. It can be seen that their similar crystal structures result in the same angle dependence of mobility; both C₆-PyDI and C₅-PyDI show remarkable anisotropic behavior and the highest mobility values appear when the value of Φ is near 0/180°, that is, along the crystallographic *b* axis. This mobility distribution as a function of Φ is consistent with their one-dimensional molecular packing character. The ranges of mobility values of C₅-PyDI and C₆-PyDI estimated in the same layer are summarized in Table 3. We can see that the ranges of the hole- and electron-mobility values in C₅-PyDI and C₆-PyDI crystals agree well with the experimental measurements by Wu *et al.* (2017), which verifies the rationality of our computational method and strategy. Comparison of the predicted hole and electronic mobility values for C₅-PyDI and C₆-PyDI indicates that the holes in C₅-PyDI are intrinsically more mobile than the holes in C₆-PyDI; while for the electron, the mobility values in the crystal of C₅-PyDI are obviously lower than those in C₆-PyDI. Combined with the experimental results reported recently, it can be seen that the hole- and electron-transfer mobilities of C₅-PyDI and C₆-PyDI in the experiments of Wu *et al.* (2017) might have reached their optimum values as *n*-type or ambipolar materials.

For *t*-C₅-PyDI, we simulated the angular resolution anisotropic mobility for both electron and hole transport. As shown in Fig. 4(b), it can be seen that the hole- and electron-transfer mobility values in the *ab* plane show

Table 4

VIPs, AIPs, VEAs and AEAs calculated at the B3LYP/6-311** level (eV).

Molecules	VIP	AIP	VEA	AEA
C ₅ -PyDI	7.59	7.51	1.87	2.00
C ₆ -PyDI	7.59	7.51	1.88	2.01
<i>t</i> -C ₅ -PyDI	7.34	7.25	1.84	1.96
<i>t</i> -C ₆ -PyDI	7.32	7.23	1.83	1.95

similar anisotropic behavior: the highest and lowest mobility values were present at $\Phi = 0/180^\circ$ and $\Phi = 90/270^\circ$, respectively. The maximum hole-transfer mobility value is only $0.004 \text{ cm}^2 \text{ s}^{-1} \text{ V}^{-1}$, and the maximum electron-transfer mobility value is less than $0.0001 \text{ cm}^2 \text{ s}^{-1} \text{ V}^{-1}$, which is consistent with the reported highest electron transport mobility ($8.72 \times 10^{-5} \text{ cm}^2 \text{ s}^{-1} \text{ V}^{-1}$). Although the introduction of the *t*-butyl group has very slight effects on the reorganization energy associated with charge-carrier transfer, the steric effect induced by its large volume dramatically changes the relative position between adjacent molecules, which has a large interference on the size of V_h and V_e values. As a result, the OFETs fabricated from *t*-C₅-PyDI exhibited lower conductive performance.

3.4. Ionization potential and electronic affinity

Aside from mobility, charge injection efficiency is also an important factor that affects the performance of an OFET device, especially for the ambipolar and *n*-channel OFETs. For OFETs, it requires that the electrode materials have work functions suited for the injection of holes/electrons into the HOMO/LUMO of semiconductor molecules. In molecular orbital theory approaches, the HOMO energy is related to the IP by Koopmanns' theorem and the LUMO energy is used to estimate the electron affinity ($-E_{\text{HOMO}} = \text{IP}$ and $-E_{\text{LUMO}} = \text{EA}$); however, the $-E_{\text{HOMO}}/ -E_{\text{LUMO}}$ values are usually inconsistent with IP/EA values in the practical DFT calculations, partly due to the unknown 'exact' exchange-correlation functional. Previous calculations by Zhan *et al.* showed that the directly calculated vertical IPs are, on the whole, in good agreement with the corresponding experimental IPs (Zhan *et al.*, 2003). Thus, we select IP and EA values of the studied compounds as the evaluation parameters to analyze the charge-injection barrier of the OFET.

For the metal electrode, the key for efficient injection of charge-carrier is that the IP values should be close to or smaller than the work function of the metal electrode; and the EA values should be close to or larger than the work function of the metal electrode. Considering the thermal and oxidative stability of electron-transport materials, the suitable EA values need to be at least 2.8 eV (Newman *et al.*, 2004). The calculated IPs and EAs of C₅-PyDI, C₆-PyDI, *t*-C₅-PyDI and *t*-C₆-PyDI are shown in Table 4. We can see that the AIP values of C₅-PyDI, C₆-PyDI, *t*-C₅-PyDI and *t*-C₆-PyDI are larger than 7.0 eV. In this case, it needs a strong external electric field to overcome the high hole-injection barriers. It is noteworthy that the introduction of the *t*-butyl group in C₅-PyDI and C₆-PyDI could decrease their AIP values by 0.25 and 0.27 eV, respectively, which is favorable for hole injection. For the

Table 5

Electronic excitation energies (λ), oscillator strengths (f), corresponding compositions and the configuration interactions (CI) for *t*-C₅-PyDI in gas and in cyclohexane.

	Transition	λ (nm)	f	Composition	CI (%)
<i>t</i> -C ₅ -PyDI (gas)	$S_0 \rightarrow S_1$	383	0.201	H → L	91
	$S_0 \rightarrow S_{10}$	268	0.471	H → L + 2	79
<i>t</i> -C ₅ -PyDI (cyclohexane)	$S_0 \rightarrow S_1$	392	0.287	H → L	100
	$S_0 \rightarrow S_3$	350	0.129	H - 1 → L	85
	$S_0 \rightarrow S_9$	271	0.595	H → L + 2	82

predicted EA values, it is observed that (i) all AEA values of C₅-PyDI, C₆-PyDI, *t*-C₅-PyDI and *t*-C₆-PyDI are larger than 1.9 eV, suggesting PyDI can be selected as electron-deficient frameworks for *n*-type or ambipolar semiconductors; and (ii) addition of the *t*-butyl group causes a slight decrease in AEA values of C₅-PyDI and C₆-PyDI, which is unfavorable to the electron-injection process.

3.5. Electronic spectra

Based on the optimized geometries, we simulated the UV-vis absorption spectra of *t*-C₅-PyDI in the gas phase and in chloroform solvent, as shown in Fig. 5(a). It can be seen that the calculated absorption peak positions in chloroform solvent are similar to the case in the gas phase. Their maximum absorption bands are observed in the near-UV region, which is consistent with the experimental excitation wavelength (270 nm) obtained by Wu *et al.* (2017). To gain a deeper understanding of the spectra character, the excited states and the frontier molecular orbitals (FMOs) were analyzed in detail, which can provide information about the nature of the excited-state conformations. For *t*-C₅-PyDI in chloroform, as shown in Table 5, there exists an $S_0 \rightarrow S_1$ transition at 392 nm, an $S_0 \rightarrow S_3$ transition at 350 nm and an intense $S_0 \rightarrow S_9$ transition at 271 nm. The S_1 state of *t*-C₅-PyDI is mainly formed by the transitions from the HOMO to the LUMO; the S_3 and S_9 states are predominantly formed by the transitions from HOMO-1 to the LUMO, and by the transitions from the HOMO to LUMO+2, respectively. Moreover, the fluorescence spectrum of *t*-C₅-PyDI is also simulated and the results are shown in Fig. 5(b). It is found that the predicted fluorescence maximum of *t*-C₅-PyDI, corresponding to the $S_1 \rightarrow S_0$ transition process, is located at 485 nm, which is quite close to the experimental value of 480 nm (Wu *et al.*, 2017).

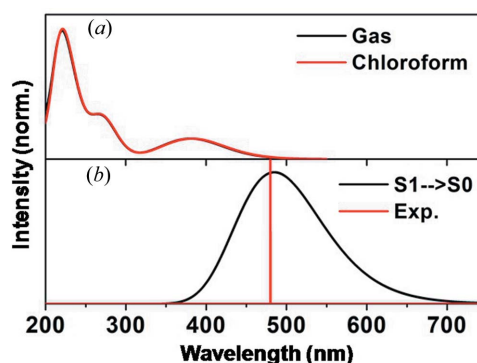


Figure 5

(a) Calculated absorption spectra of *t*-C₅-PyDI in gas and in chloroform. (b) Calculated fluorescence spectra of *t*-C₅-PyDI in cyclohexane.

4. Conclusions

In this manuscript, we simulated anisotropic charge-transfer mobilities of C₅-PyDI, C₆-PyDI and *t*-C₅-PyDI, and theoretically predicted the range of their mobility values, which provided reference for the performance optimization of an OFET based on these materials. We systematically analyzed the influences of the alkyl chain on the reorganization energies, crystal packing, electronic couplings and charge injection barrier of PyDI. It is found that the introduction of alkyl chain groups into PyDI has little effect on the reorganization energy, but increases the repulsive interactions of the backbone and thus affects the molecular packing in the crystal. As a result, the electrons in the *t*-C₅-PyDI crystal are intrinsically less mobile than the electrons in the C₅-PyDI crystal. Moreover, the alkyl chain substitution could decrease the electronic affinities and ionization potentials, which decreases the hole-injection barrier and improves the injection efficiency of the holes. We also simulated electronic spectra of *t*-C₅-PyDI which reproduced the experimental absorption and fluorescence spectra well.

Funding information

This work was supported by the National Science Foundation of China (grant Nos. 81601825, 21503034), the Taishan Scholars project of Shandong Province (grant No. ts201712011), Fundamental Research Funds for the Central Universities (grant No. wd01156), Program for Science and Technology Project of Liaoning Province (grant No. 201601237), Educational Committee Foundation of Liaoning Province (grant No. L2015150), and the Initial Funds for Imported Talents' Research Projects, Dalian Nationalities University (grant No. 20136131).

References

- Bélanger-Chabot, G., Ali, A. & Gabbai, F. P. (2017). *Angew. Chem. Int. Ed.* **56**, 9958–9961.
- Ford, M. J., Wang, M., Patel, S. N., Phan, H., Segalman, R. A., Nguyen, T. & Bazan, G. C. (2016). *Chem. Mater.* **28**, 1256–1260.
- Frisch, M. J. *et al.* (2009). *GAUSSIAN09*. Gaussian Inc., Pittsburgh, Pennsylvania, USA.
- Gao, Y., Deng, Y., Tian, H., Zhang, J., Yan, D., Geng, Y. & Wang, F. (2017). *Adv. Mater.* **29**, 1606217.
- Haughey, A.-M., McConnell, G., Guilhabert, B., Burley, G. A., Dawson, M. D. & Laurand, N. (2016). *IEEE J. Sel. Top. Quantum Electron.* **22**, 1300109.
- Huang, J.-D., Li, W.-L., Wen, S.-H. & Dong, B. (2015). *J. Comput. Chem.* **36**, 695–706.
- Huang, J.-D., Teng, W., Chen, D. & Ma, H. (2018). *J. Mol. Liq.* **249**, 957–962.
- Huang, J.-D., Yu, K., Ma, H., Chai, S. & Dong, B. (2017a). *Dyes Pigments*, **141**, 441–447.
- Huang, J.-D., Zhang, J., Chen, D. & Ma, H. (2017b). *Org. Chem. Front.* **4**, 1812–1818.
- Klamt, A. & Schüürmann, G. (1993). *J. Chem. Soc. Perkin Trans. 2*, **0**, 799–805.
- Kobaisi, M. A., Bhosale, S. V., Latham, K., Raynor, A. M. & Bhosale, S. V. (2016). *Chem. Rev.* **116**, 11685–11796.
- Kuehne, A. J. C. & Gather, M. C. (2016). *Chem. Rev.* **116**, 12823–12864.
- Lee, C. T., Yang, W. T. & Parr, R. G. (1988). *Phys. Rev. B*, **37**, 785–789.
- Li, W., Hendriks, K. H., Wienk, M. M. & Janssen, R. A. J. (2016). *Acc. Chem. Res.* **49**, 78–85.
- Lin, G., Peng, H., Chen, L., Nie, H., Luo, W., Li, Y., Chen, S., Hu, R., Qin, A., Zhao, Z. & Tang, B. Z. (2016). *Appl. Mater. Interfaces*, **8**, 16799–16808.
- Liu, C., Xiao, C., Li, Y., Hu, W., Li, Z. & Wang, Z. (2014). *Chem. Commun.* **50**, 12462–12464.
- Ma, H., Chai, S., Chen, D. & Huang, J.-D. (2017a). *IUCrJ*, **4**, 695–699.
- Ma, H. & Huang, J.-D. (2016). *RSC Adv.* **6**, 96147–96153.
- Ma, H., Liu, N. & Huang, J.-D. (2017b). *Sci. Rep.* **7**, 1–12.
- Matsushima, T., Hwang, S., Sandanayaka, A. S. D., Qin, C., Terakawa, S., Fujihara, T., Yahiro, M. & Adachi, C. (2016). *Adv. Mater.* **28**, 10275–10281.
- Newman, C. R., Frisbie, C. D., da Silva Filho, D. A., Brédas, J. L., Ewbank, P. C. & Mann, K. R. (2004). *Chem. Mater.* **16**, 4436–4451.
- Purdum, G. E., Yao, N., Woll, A., Gessner, T., Weitz, R. T. & Loo, Y.-L. (2016). *Adv. Funct. Mater.* **26**, 2357–2364.
- Raghuwanshi, V., Bharti, D. & Tiwari, S. P. (2016). *Org. Electron.* **31**, 177–182.
- Skrypnichuk, V., Wetzelaer, G. A. H., Gordiichuk, P. I., Mannsfeld, S. C. B., Herrmann, A., Toney, M. F. & Barbero, D. R. (2016). *Adv. Mater.* **28**, 2359–2366.
- Stolte, M., Suraru, S.-L., Diemer, P., He, T., Burschka, C., Zschieschang, U., Klauk, H. & Würthner, F. (2016). *Adv. Funct. Mater.* **26**, 7415–7422.
- Sung, M. J., Luzio, A., Park, W.-T., Kim, R., Gann, E., Maddalena, F., Pace, G., Xu, Y., Natali, D., de Falco, C., Dang, L., McNeill, C. R., Caironi, M., Noh, Y.-Y. & Kim, Y.-H. (2016). *Adv. Funct. Mater.* **26**, 4984–4997.
- Tang, A., Zhan, C., Yao, J. & Zhou, E. (2017). *Adv. Mater.* **29**, 1600013.
- Te Velde, G., Bickelhaupt, F. M., Baerends, E. J., Guerra, C. F., Van Gisbergen, S. J. A., Snijders, J. G. & Ziegler, T. (2001). *J. Comput. Chem.* **22**, 931–967.
- Treutler, O. & Ahlrichs, R. (1995). *J. Chem. Phys.* **102**, 346–354.
- Wang, Z., Huang, L., Zhu, X., Zhou, X. & Chi, L. (2017). *Adv. Mater.* **29**, 1703192.
- Wu, Z.-H., Huang, Z.-T., Guo, R.-X., Sun, C.-L., Chen, L.-C., Sun, B., Shi, Z.-F., Shao, X., Li, H. & Zhang, H.-L. (2017). *Angew. Chem. Int. Ed.* **56**, 13031–13035.
- Würthner, F. & Stolte, M. (2011). *Chem. Commun.* **47**, 5109–5115.
- Xu, X., Yao, Y., Shan, B., Gu, X., Liu, D., Liu, J., Xu, J., Zhao, N., Hu, W. & Miao, Q. (2016). *Adv. Mater.* **28**, 5276–5283.
- Yang, D., Wu, J., Dong, H., Jia, M. & Song, X. (2018). *J. Phys. Org. Chem.* **31**, e3756.
- Yang, D., Zhao, J., Yang, G., Song, N., Zheng, R. & Wang, Y. (2017). *J. Mol. Liq.* **241**, 1003–1008.
- Yang, Y., Zhang, Z.-G., Bin, H., Chen, S., Gao, L., Xue, L., Yang, C. & Li, Y. (2016). *J. Am. Chem. Soc.* **138**, 15011–15018.
- Yao, J., Yu, C., Liu, Z., Luo, H., Yang, Y., Zhang, G. & Zhang, D. (2016). *J. Am. Chem. Soc.* **138**, 173–185.
- Yi, Z., Wang, S. & Liu, Y. (2015). *Adv. Mater.* **27**, 3589–3606.
- Yin, S., Li, L., Yang, Y. & Reimers, J. R. (2012). *J. Phys. Chem. C*, **116**, 14826–14836.
- Yin, S. & Lv, Y. (2008). *Org. Electron.* **9**, 852–858.
- Yuan, Z., Ma, Y., Geßner, T., Li, M., Chen, L., Eustachi, M., Weitz, R. T., Li, C. & Müllen, K. (2016). *Org. Lett.* **18**, 456–459.
- Yue, W., Jiang, W., Böckmann, M., Doltsinis, N. L. & Wang, Z. (2014). *Chem. Eur. J.* **20**, 5209–5213.
- Zhan, C. G., Nichols, J. A. & Dixon, D. A. (2003). *J. Phys. Chem. A*, **107**, 4184–4195.
- Zhang, M.-X. & Zhao, G.-J. (2012). *ChemSusChem*, **5**, 879–887.
- Zhang, W., Yao, J. & Zhao, Y. S. (2016). *Acc. Chem. Res.* **49**, 1691–1700.
- Zhao, Y. & Liang, W. (2012). *Chem. Soc. Rev.* **41**, 1075–1087.
- Zhao, Z., Yin, Z., Chen, H., Zheng, L., Zhu, C., Zhang, L., Tan, S., Wang, H., Guo, Y., Tang, Q. & Liu, Y. (2017). *Adv. Mater.* **29**, 1602410.